Research Article

Investigation of mechanical failure performance of a large-diameter shield tunnel segmental ring

Binyong GAO[1,2], Renpeng CHEN[1,2], Huaina WU[1,2✉], Chengcheng ZHANG[1,2], Meng FAN[1,2], Chao XIAO[3]

[1]*Research Center of Underground Space Advanced Technology, Hunan University, Changsha 410082, China*
[2]*Key Laboratory of Building Safety and Energy Efficiency of the Ministry of Education, Hunan University, Changsha 410082, China*
[3]*China Construction No. 5 Civil Engineering Co., LTD., Changsha, China*

Abstract: The control criteria for structural deformation and the evaluation of operational safety performance for large-diameter shield tunnel segments are not yet clearly defined. To address this issue, a refined three-dimensional finite element model was established to analyze the transverse deformation response of a large-diameter segmental ring. By analyzing the stress, deformation, and crack distribution of large-diameter segments under overload conditions, the transverse deformation of the segmental ring could be divided into four stages. The main reasons for the decrease in segmental ring stiffness were found to be the extensive development of cracks and the complete formation of four plastic hinges. The deformation control value for the large-diameter shield tunnel segment is chosen as 8‰ of the segment's outer diameter, representing the transverse deformation during the formation of the first semi-plastic hinge (i.e., the first yield point) in the structure. This control value can serve as a reinforcement standard for preventing the failure of large-diameter shield tunnel segments. The flexural bearing capacity characteristic curve of segments was used to evaluate the structural strength of a large-diameter segmental ring. It was discovered that the maximum internal force combination of the segment did not exceed the segment ultimate bearing capacity curve (SUBC). However, the combination of internal force at $9°$, $85°$, $161°$ of the joints, and their symmetrical locations about the $0°\sim180°$ axis exceeded the joint ultimate bearing capacity curve (JUBC). The results indicate that the failure of the large-diameter segment lining was mainly due to insufficient joint strength, leading to an instability failure. The findings from this study can be used to develop more effective maintenance strategies for large-diameter shield tunnel segments to ensure their long-term performance.

Key words: Finite element model; Transverse deformation response; Upper overload; Plastic hinges; Flexural bearing capacity

1 Introduction

In recent decades, there has been significant progress and remarkable development in shield tunnel construction technology in China(Yan et al., 2022, 2023; Shen et al., 2023a). The worldwide development of urban subway, highway and railway tunnels has driven the use of large-diameter shield tunnelling in construction(Han et al., 2017; Liu et al., 2017b; Chen et al., 2019; Zhang et al., 2021). Examples of such tunnels include the Shanghai Dapu Road Tunnel with an outer diameter of 10.0 m, the Shanghai Yangtze River Tunnel with an outer diameter of 15.0 m, and the upcoming Chunfeng Road Tunnel with an outer diameter of 15.4 m (He et al., 2021). Precast reinforced concrete segments connected by bolts form the main load-bearing structure of the shield segment linings. However, large deformations of the segment lining may occur during operation due to construction activities in the vicinity of the tunnel, such as excavation and overloading (Wu et al., 2020; Meng et al., 2021; 2022). Therefore, problems like excessive convergence, concrete spalling, groundwater leakage, and segment cracking (Chang et al., 2001; Yuan et al., 2013; Li et al., 2014; Chen et al., 2016; Gong and Ding, 2018; Shen et al., 2023b; Zhang et al., 2023b) can affect the safe operation of the tunnel and even have catastrophic consequences. There is currently detailed research available on deformation control standards for small-diameter shield tunnel segments. However, it is uncertain how to evaluate operational

✉ Huaina Wu, wuhn@hnu.edu.cn
🆔 Huaina Wu, https://orcid.org/0000-0001-7359-3669

safety performance and structural deformation control criteria for large-diameter shield tunnel segments. Therefore, the failure mechanism and deformation law of the large-diameter shield tunnel segment lining under external load are well worth thorough investigation.

The methods of simplified mechanical model analysis, full-scale experiments and numerical analysis are employed to study the mechanical behavior and failure properties of the segment lining. For simplified mechanical model analysis, previous researchers have used various theoretical models to investigate the bending stiffness of segment joints, as in the work of Li et al. (2015); Zhang et al. (2019b); Wang et al. (2020); Yang et al. (2020); Qiu et al. (2021). Although these models have made significant progress in understanding the mechanical behavior of segment joints, there is still a lack of description of the deformation and failure mechanism of the segment ring structure. There are two main types of model for the segmental ring: the homogeneous circular ring method and the beam-spring model. The homogeneous circular ring method assumes that the segmental ring is a uniform and isotropic circular ring, and considers the influence of bending stiffness at the joint by introducing a reduction coefficient (Koyama and Nishimura, 1998; Lee and Ge, 2001; Liao et al., 2008; Huang et al., 2012). However, that model fails to describe the mechanical effects between the segment joints. Several researchers (Murakami and Koizumi, 1978; Ding et al., 2003; Zhao et al., 2017) have attempted to compensate for this shortcoming by assuming that the segments are beams and that the joints are idealized as a series of tension and rotation springs. In beam-spring models, it is very difficult to determine the properties of the spring and the spring stiffness is commonly oversimplified as a constant.

Researchers have conducted full-scale experiments to investigate the deformation and failure mechanisms of segmental ring and joint in recent years (Blom et al., 1999; Liu et al., 2015, 2017a, 2018; Feng et al., 2018; Qiu, et al., 2021). Zhang et al. (2019a) conducted prototype experiments to study and summarize the failure characteristics of a shield tunnel segment lining with through straight joint assembly and staggered joint assembly under high water pressure. Liu et al. (2020) studied the load-bearing capacity of peripheral unloading segmental rings

through a series of full-scale experiments. The experimental results describe the progressive failure mechanism and ultimate load-bearing capacity of single and multiple ring structures. Wei et al. (2022) performed a full-scale loading experiment of a three-ring staggered assembly of the shield tunnel segments for the Hangzhou metro to investigate the structural performance and failure process of the segments under asymmetric unloading. For large-diameter shield tunnel segments, it is extremely challenging to conduct full-scale experiments due to the limitations of loading equipment conditions. Currently, some scholars have conducted joint experiments on large-diameter segments, but the joint experiments cannot analyze the overall deformation mechanism of the segmental ring (Liu et al., 2022; Zhang et al., 2022; Guo et al., 2023).

Considering factors such as the vast time, high cost and limited data obtained by full-scale experiments, numerical simulation has become an alternative method for investigating the mechanical behavior of segment linings (Cavalaro et al., 2011; Arnau and Molins, 2015; Wang et al., 2019; Chen et al., 2020; Wu et al., 2022). The segment linings were mostly simulated using the shell element in the beginning because of both the hardware and software restrictions in the computational technology, whereas segment joints were simulated generally using continuum medium elements or nonlinear surface elements (Arnau and Molins, 2012; Yan et al., 2018). Such simplified numerical models can reproduce the segment internal forces and deformations but fail to express the realistic behavior of segment joints, such as the joint opening, rotational angle and bending stiffness (Li et al., 2016). Therefore, the refined 3D finite element model was developed to study the mechanical behavior and bearing mechanism of shield segments linings (Chen and Mo, 2008, 2009; Ding et al., 2014; Jin et al., 2017). At present, the research on the failure mechanism of shield segment lining through numerical simulation is mostly for small-diameter segments. Only few scholars (Feng, et al., 2018; Zhang et al., 2020, 2023a) have researched the joint performance of large-diameter shield tunnel segments without conducting in-depth research on the entire segmental ring.

Compared to the small-diameter shield tunnel segment, the large-diameter shield tunnel segments

exhibit significantly different structural characteristics, which make their mechanical properties different. The increase in the number of segment blocks and joints in large-diameter tunnel segments not only significantly affects the overall structural stiffness but also has a considerable impact on the stress distribution within the structure. This is because the joints are the vulnerable areas of the entire segment ring and they can profoundly influence its structural stress and deformation. Large-diameter tunnel segments typically have greater height and width, leading to a more complex spatial distribution of internal forces and deformations throughout the structure. Due to their larger cross-sectional area, large-diameter tunnel segments often need to withstand higher soil and water loads. Consequently, the deformation mechanisms of large-diameter tunnel segments are more intricate and require in-depth research and analysis.

In this paper, a refined 3D finite element analysis was performed on the segment lining of a large-diameter shield tunnel to evaluate its structural transverse deformation behavior and mechanical mechanism. First of all, the transverse deformation, the internal force, crack development, bolt and reinforcement stress, concrete compressive strain and longitudinal joint opening of the large-diameter segment ring were determined. Moreover, the development process of macroscopic performance points was analyzed, along with the reasons for the decrease in structural stiffness of large-diameter segmental rings under overload conditions. Finally, the internal force of the segmental ring is brought into the characteristic curve of the flexural bearing capacity of the segment.

2 Numerical Model

2.1 Project overview

The numerical model is established based on the Wanghai Road Highway Tunnel in Shenzhen, China. The tunnel is constructed using precast reinforced concrete (RC) segments with a concrete grade of C60. The longitudinal joints between segments are connected by two 8.8 grade M39 oblique bolts. The segment lining reinforcement cage is mainly composed of main bars and stirrups. The main bars are HRB400 (GB/T 28900, 2022) with diameters of 20 mm, 25 mm and 28 mm respectively, and the stirrups

are HPB300 with diameters of 8 mm. The outer diameter of the segment is 15.7 m, the thickness is 0.65 m, and the segment ring width is 1.5 m. The segment lining adopts the block method of "7+2+1", that is 1 key segment, 2 adjacent segments and 7 standard segments. The central angle of the key segment is 12°51′26″, while the central angle of other segments is 38°34′17″, as shown in Fig. 1(a). We select a certain unfavorable stratum section as the external load for the segment design, as shown in Fig. 1 (b). The parameters of the most unfavorable stratum are shown in Table 1. The thickness of the overlying soil layer of the tunnel is 22.04 m, and the tunnel is located in a sandy soil layer.

Table 1 Design parameters of the most unfavorable stratum

Parameters	Values	Parameters	Values
Buried depth H	22.04 m	Groundwater level H_w	2.7 m
Ground overload p_0	20 kN/m²	Lateral earth pressure coefficient	0.35

2.2 Finite element model

Fig. 2 shows the established sophisticated 3D solid finite-element model of the large-diameter reinforced concrete segment. The numerical model includes reinforced cage, concrete and connecting bolts. By setting appropriate material properties and establishing the interaction between the segment and the bolts, the real deformation behavior of the segment can be simulated. The segments and connecting bolts are modelled as linear solid elements having eight nodes (C3D8R). The reinforcing rebars were modelled as 3D stress/displacement truss elements (T3D2). The number of elements in the numerical model of the segment is 188711, and the number of nodes is 225326.

Referring to the boundary constraints of the entire ring full-scale experiment done by Liu, et al. (2017b), the single-ring segment was assumed to be a simply supported beam. The boundary condition constraints of the segment lining were realized by fixing the displacement of the longitudinal grid node of the outer surface in the X direction at 0° (roller supports), the displacement of the longitudinal grid node of the outer surface in the X and Y directions at 180° (pin supports), and the displacement of the circumferential joint surface in the Z direction is constrained by the roller support, as shown in Fig. 2.
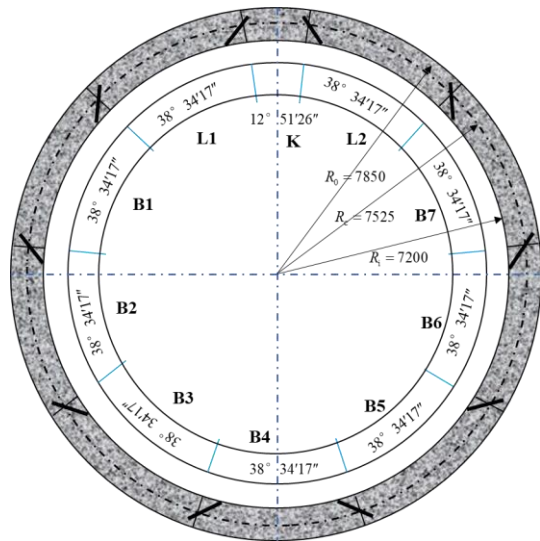
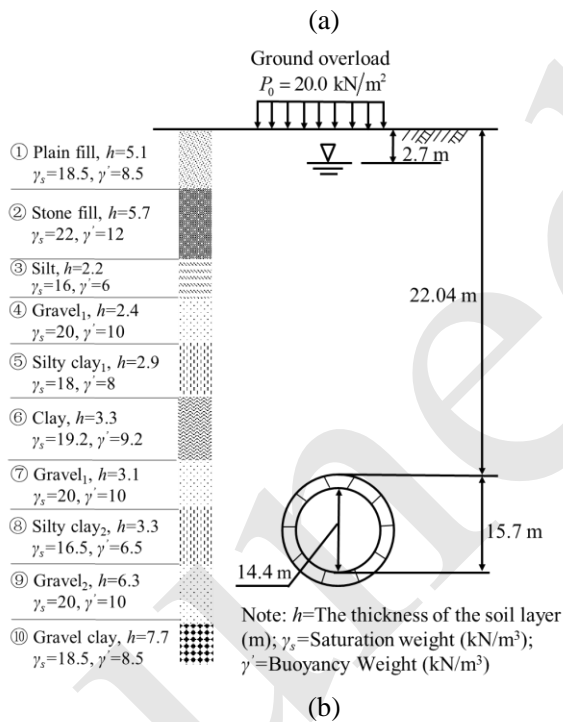Note: K=key segments, L1, L2=adjacent segments, B1~B7= standard segments.

(a)

(b)

Fig. 1 Wanghai Road Tunnel reinforced concrete segment design: (a) reinforced concrete segment block diagram; (b) outline drawing of stratum design

A surface-to-surface contact was applied to simulate the interaction between adjacent segments. The tangential behavior of this contact adopts a penalty function, the normal behavior adopts a hard contact, and the friction coefficient value is taken as 0.55 (Zhang, et al., 2020; Huang et al., 2021). The maximum allowable elastic slip is 0.005 of the char-

acteristic surface dimensions. The contacts are designated non-penetration and allowed to separate, the normal compression and tension are supported by the contacts. The rebar was embedded as constraints in the concrete structure to simulate the bond relationship between the rebar and concrete. The contact relationship between the bolts and the segments primarily utilizes the surface-to-surface contact simulation method. A friction coefficient of 0.15 has been applied between the screws and the concrete, while the interaction between the nut and the concrete was set as a binding contact, as shown in Fig. 2.
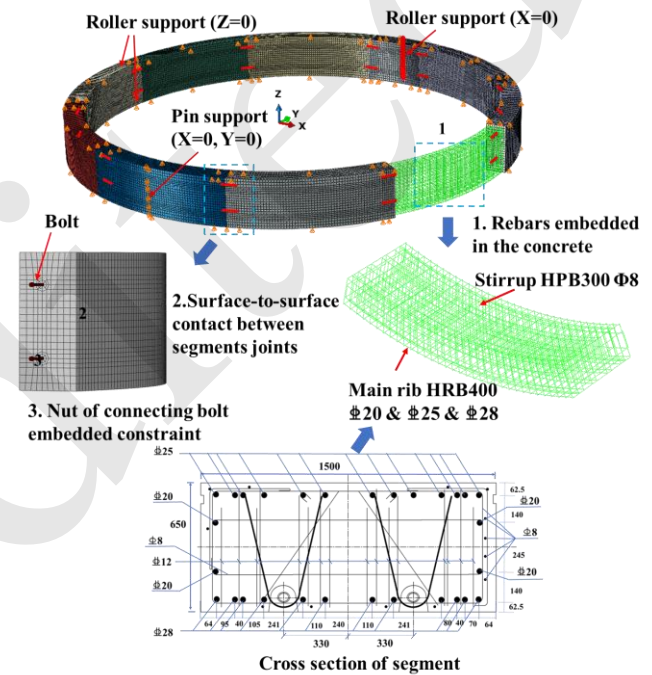

Fig. 2 3D FEA model of large-diameter shield tunnel segment

2.3 Constitutive models and parameters

The concrete grade of the reinforced concrete segment is taken as C60, and the concrete damage plasticity (CDP) model is applied to the simulation. The constitutive model uses isotropic elastic damage combined with isotropic tension and compressive plasticity to represent the inelastic behavior of concrete. It is based on the assumption of the same failure in all directions and assumes that the primary failure mechanisms of concrete are tension cracking and compressive crushing (Dassault Systèmes, 2016). The CDP model of concrete material parameters is listed in Table 2. The compression and tension failure behavior of concrete C60 is depicted in Fig. 3. The

stress-strain curve is determined according to the Chinese Code for Design of Concrete Structured GB 50010-2010, and the plastic damage factor is calculated by reference to the method proposed by Birtel and Mark (2006).

The main reinforcing bars are set at HRB 400 with its yield strength of 400 MPa, and the stirrup adopts HPB 300 with its yield strength of 300 MPa. The tensile strength of the connected high-strength prestressed bolt M39 is 640 MPa, and the yield ratio is 0.8. The ideal elastoplastic model was selected to describe the mechanical behavior of reinforcing rebars and connecting bolts. The material parameters are shown in Table 3.

**Table 2 Parameters of Concrete Damage Plasticity model for concrete C60**

Parameters	Values	Parameters	Values
Mass Density ρ (kg/m3)	2440	Invariant stress ratio K_c	0.6667
Young's Modulus E (GPa)	36	Viscosity Parameter μ	0.0005
Poisson's Ratio v	0.2	Biaxial/uniaxial compression plastic strain ratio f_{b0}/f_{c0}	1.16
Dilation Angle ψ (°)	38	Flow potential eccentricity	0.1

Table 3 Material parameters of bolts and reinforcement

Material	Elastic Modulus (GPa)	Poisson's Ratio v	Yield Strength (MPa)
HPB 300	210	0.3	300
HRB 400	200	0.3	400
Bolt	200	0.3	640
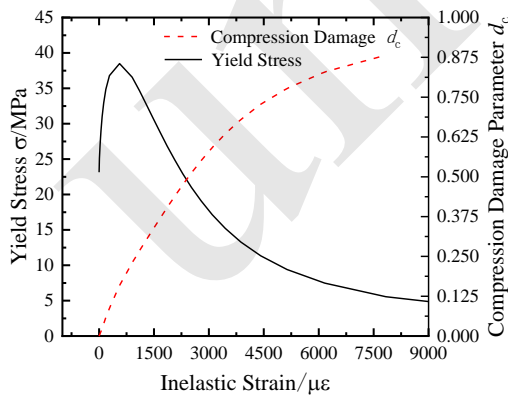
(a)
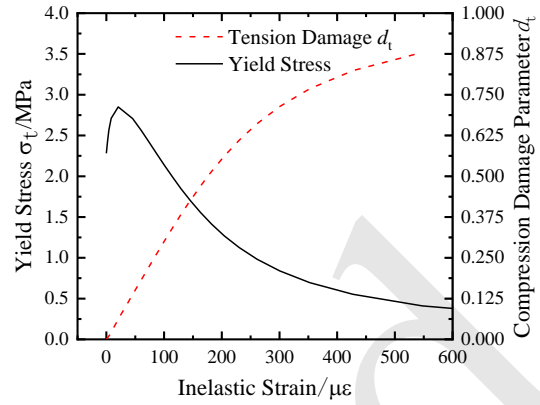
(b)

Fig. 3 Damage behavior of concrete C60: (a) compression damage; (b) tension damage

2.4 Loading procedure

The full-scale experiment of the segmental ring simulates water and soil pressure, soil resistance and ground overload, by arranging a number of jacks around the full-ring segment to apply horizontal radial loads to the specimen. The principle of experimental concentrative force design is that the equivalent load is applied by the jack to replace the actual pressure on the segment. At this point, the internal force of the key sections of the segment ring is the same as that under the design load. The test setup is a self-balancing loading system which includes fixed beams, jacks, distributing beams and anchor bars. The steel 44 bars are all anchored in the center of the lining and, for each loading point, crossbeams anchored at the bar ends provide counter for the jacks. The application position of the horizontal equivalent load is depicted in Fig.4 (a). The loads acting on the lining ring are simplified as 44 concentrated forces directed to the center of the circle equally divided by the center angle, including 10 loads P_1, 12 loads P_2, 12 loads P_3 and 10 loads P_4. Actually, this principle was also used in previous structure-level tests for segmental linings (Nakamura et al., 2003; Lu et al., 2011). As shown in Fig. 4(b), the loading process for the overburden condition is divided into two stages as shown below:

(1) Stage I: Gradually P_4 increased from 0 to 1640 kN (passive earth pressure); P_1, P_2 and P_3 increase simultaneously following the principles $P_1 = 1.129P_4, P_2 = 0.48(P_1 + P_4), P_3 = 0.446(P_1 + P_4)$.

(2) Stage II: Keeping P_4 constant at 1640 kN, P_1 continues to increase until it reaches the ultimate

bearing capacity, during the loading process $P_2 = 0.48(P_1 + P_4)$, $P_3 = 0.446(P_1 + P_4)$.
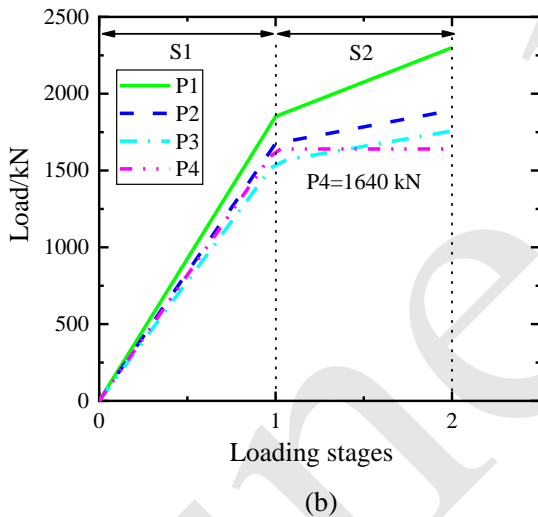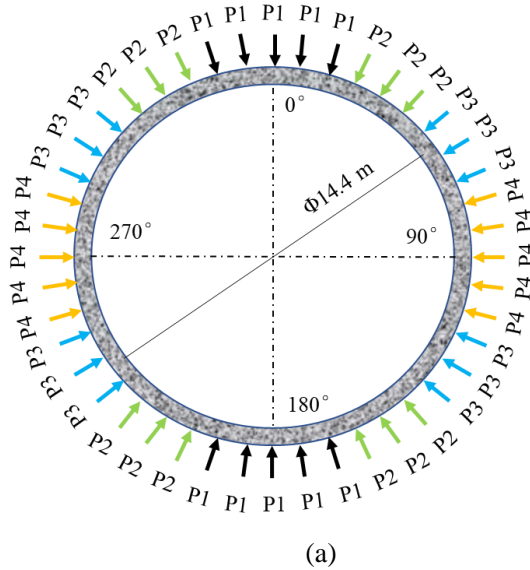

(a)

(b)

Fig. 4 Loading procedure: (a) layout of horizontal equivalent load; (b) loading stage

The finite element model establishes reference points at the corresponding angle of concentrated loads at 44 points in order to avoid the problem of stress singularity brought on by applying line load to the solid element. The concentrated load is applied directly to this geometric reference point, which establishes a coupling constraint relationship with the surface of the nearest two columns of elements.

3 Analysis of simulation results

In order to standardize and scientifically study the failure mechanism of shield tunnel linings, it is necessary to clarify the following analysis principles:

1) If the equivalent plastic strain (PEEQ) of tensile steel bar exceeds zero at any joint it is considered to have yielded. 2) When the Mises stress of the bolt at the joint reaches 640 MPa, the bolt at the joint is considered to have yielded. 3) If the principal compressive strain of the compressed concrete at a joint first reaches the maximum value and then gradually decreases, it is considered that the concrete at the joint has been crushed (Chen, et al., 2020).

Chen, et al. (2020) compared the calculation results of the established numerical model with the experimental results of Liu, et al. (2017b). The results revealed that the transverse deformation at the limit bearing capacity of the shield segment, as calculated through numerical simulations, deviates from the experimental results by only 6.2%, with relatively minor differences observed in bolt strains. This suggests that the numerical model method is reliable and reasonable. Therefore, this study adopts the same finite element modeling method and a similar loading method.

We define the difference between the top and side loads of the structural as a generalized load ($P=P_1-P_4$). The larger the generalized load, the greater the upper overload. In the following, the generalized load is used to describe the load situation of the structure.

3.1 Overall deformation

As the upper load increases, the overall deformation evolution of the segment lining structure is as shown in Fig. 5 (a). The top of the structure is concave inward at 0 °, and protrudes outward at 90 °and 270 °at the waist. The overall deformation takes the shape of a left-right symmetrical horizontal elliptical shape. This trend becomes more and more pronounced as the load increases.

Fig. 5 (b) shows how the transverse deformation of the segment changes with the gradual increase of the generalized load P. The transverse deformation of the segment is mainly divided into four stages. 1) Stage I (OA, $0 \leqslant P < 112.56$ kN): the structural deformation is in a linear growth stage, and the transverse deformation of the segmental ring at the end of this stage is 32.39 mm. 2) Stage II (IIa: AB, 112.56 kN $\leqslant P < 211.56$ kN; IIb: BC, 211.56 kN $\leqslant P < 247.79$ kN): the transverse deformation of the segment increases slowly with the increase of generalized load P and transitions from a quasi-linear growth

stage to a nonlinear growth stage. The points B and C respectively indicate that the loading method changes and the sharp intensification of segment cracks stops. The transverse deformation of segment at points B and C is 68.10 mm and 94.02 mm, respectively. 3) Stage III (CD, 247.79 kN≤P<294.87 kN): this stage is a nonlinear growth stage, where the transverse deformation continues to develop rapidly. The transverse deformation of the segment at the end of this stage reaches 246.59 mm. 4) Stage IV (DE, 294.87 kN≤P<300.1 kN): this state is the failure stage, where the transverse deformation of the segment increases very quickly. The transverse deformation of the segmental ring reached 313.95 mm at this stage.
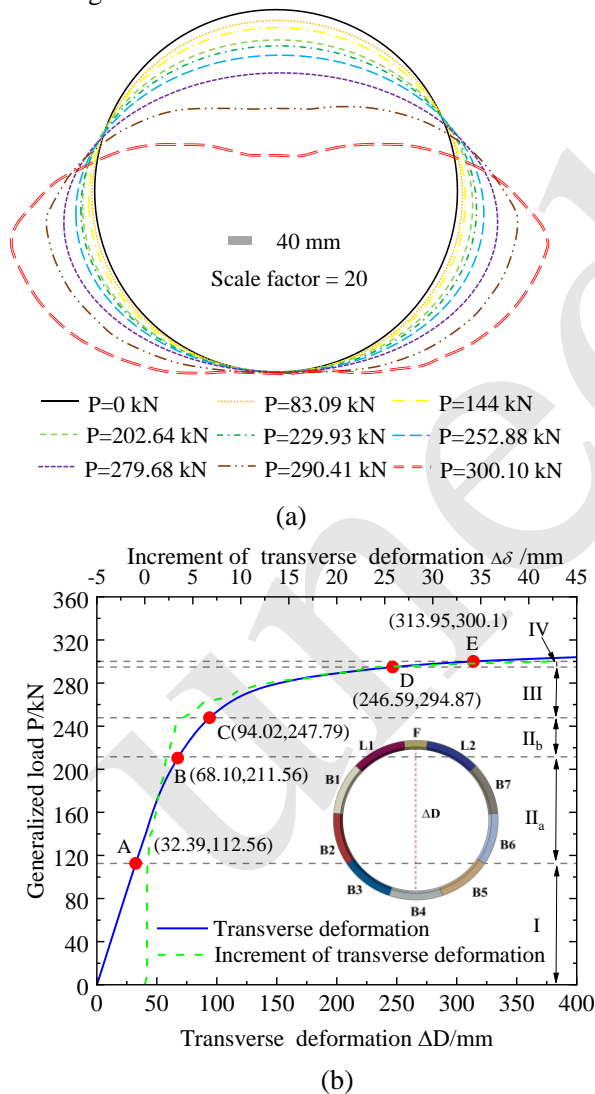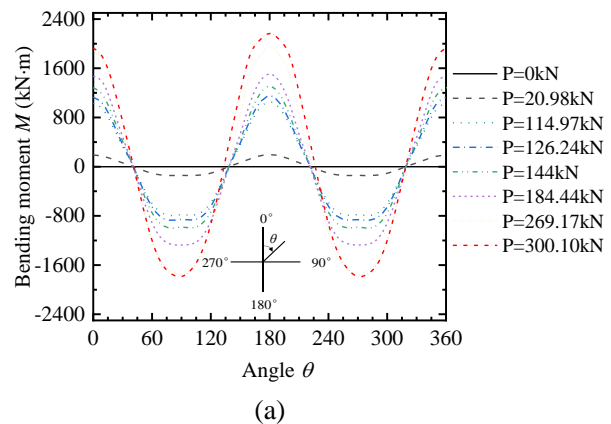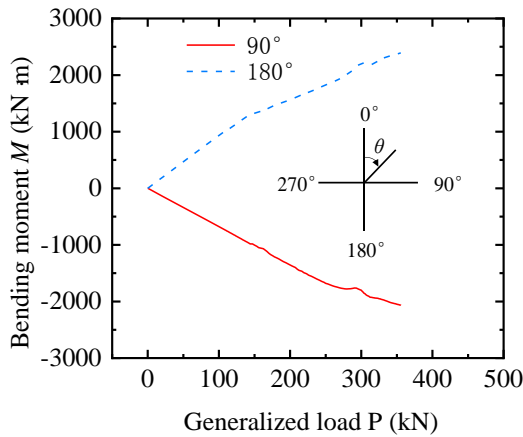
The change in the transverse deformation increment further explains the variation rule of the transverse deformation of the segmental ring. The transverse deformation increment initially remains unchanged, then increases nonlinearly, and finally, the transverse deformation increment increases rapidly. Specifically, the transverse deformation increments corresponding to the critical loads between the above stages are 0.339 mm, 2.212 mm, 3.965 mm, 24.342 mm and 42.671 mm, respectively.
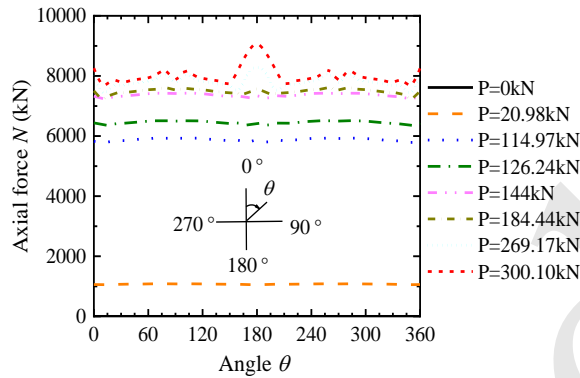
3.2 Structural internal force

Fig. 6 shows the internal force distribution of a large-diameter shield tunnel segmental ring under overload. The bending moment is defined as the outside compression and the inside tension being positive, otherwise it is negative. The axial force is positive when pointing to the section and negative when away from the section. In this study, the internal force extraction sections were set at intervals of 10° with a central angle, where the central angle (θ) was rotated clockwise from the vault. Fig. 6 (a) and (c) show that the bending moment and axial force of the large-diameter lining segment are symmetrically distributed along the line of 0~180°, with the maximum positive and negative bending moments located at 180° and 90°, respectively and the maximum axial force located at 180°. The maximum positive and negative bending moments gradually increase as the generalized load P increases and the bending moments show a "W"-shaped distribution. The axial force distribution at different positions becomes more and more obvious with the increase of load and the axial force shows a peak shaped distribution.
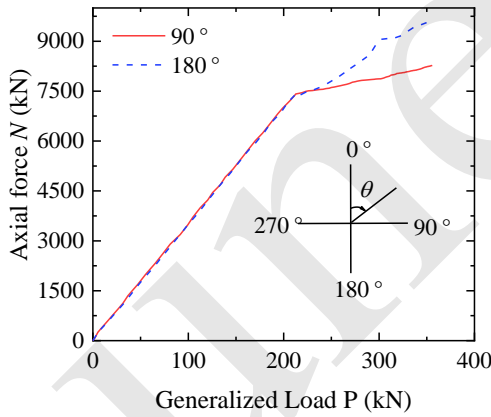

(a)

(b)

Fig. 5 Overall deformation of the segment ring: (a) segment deformation mode under overload conditions; (b) transverse deformation

(a)

(b)

(c)

(d)

Fig. 6 Distribution of internal force: (a) distribution of bending moment; (b) variation of bending moment; (c) distribution of axial force; (d) variation of axial force

Fig. 6 (b) and (d) are the bending moment and axial force variations at 90 °and 180 °, respectively. It can be seen from the figure that the positive and negative bending moments increase with the increase of generalized load *P* and the absolute value of the bending moment at 180 °is greater. Before the change of loading mode, the axial force at 90 °and 180 °re-

mained essentially unchanged, and as the load increased, the axial force at 180 °progressively exceeded the axial force at 90 °. Table 4 shows the internal force at the joint when the ultimate load *P*=300.10 kN is in the upper overload condition. The joint bending moments at 9 °, 161 °, 199 °and 351 °are positive, while the bending moments at other joints are negative. The maximum positive bending moment of the joint is at 161 °, the maximum negative bending moment is at 85 °, and the maximum axial force is at 123 °. The maximum difference of the joint axial force is 12%, and the maximum difference of the bending moment can reach 4.3 times.

3.3 Development of concrete cracking

Fig. 7 shows the crack development process of the large-diameter reinforced concrete segment under overload. In this study, the concrete tensile damage DAMAGET was selected as the evaluation index for concrete crack formation and development (Du et al., 2014; Moradloo et al., 2019). The development of concrete cracks can be divided into the following three stages:

(i) Stage A1: no concrete crack through occurs

When $0 \leqslant P < 112.56$ kN, the reinforcing rebar and the concrete of large-diameter shield segment are in an elastic state. The inner side of the segment lining is where the tensile strain reaches a maximum at 180° but there is no through crack in the width direction.

(ii) Stage A2: the number of cracks increases rapidly

When 112.56 kN$\leqslant P <$247.79 kN, the concrete cracks continue to develop rapidly as the generalized load increases. As depicted in Fig. 7(a) and (b), when the generalized load *P* reaches 112.56 kN, the segment lining forms the first through crack on the inner side of the invert. When the generalized load P reaches 177.87 kN, the first through cracks appear at the waist. Under the overload conditions, the cracks of large-diameter segments are mainly concentrated on the inner side of the lining crown (F block) and invert (B4 block) and the outer side of the spring line (B1, B2, B6, B7 block), as shown in Fig. 7(c).

(iii) Stage A3: almost no new cracks

When 247.79 kN $\leqslant P <$300.10 kN, few new concrete cracks are generated as the generalized load increases, but the depth and width of the cracks gradually increase, as illustrated in Fig. 7(d).

Table 4 Internal force at joint under ultimate load (*P*=300.10 kN)

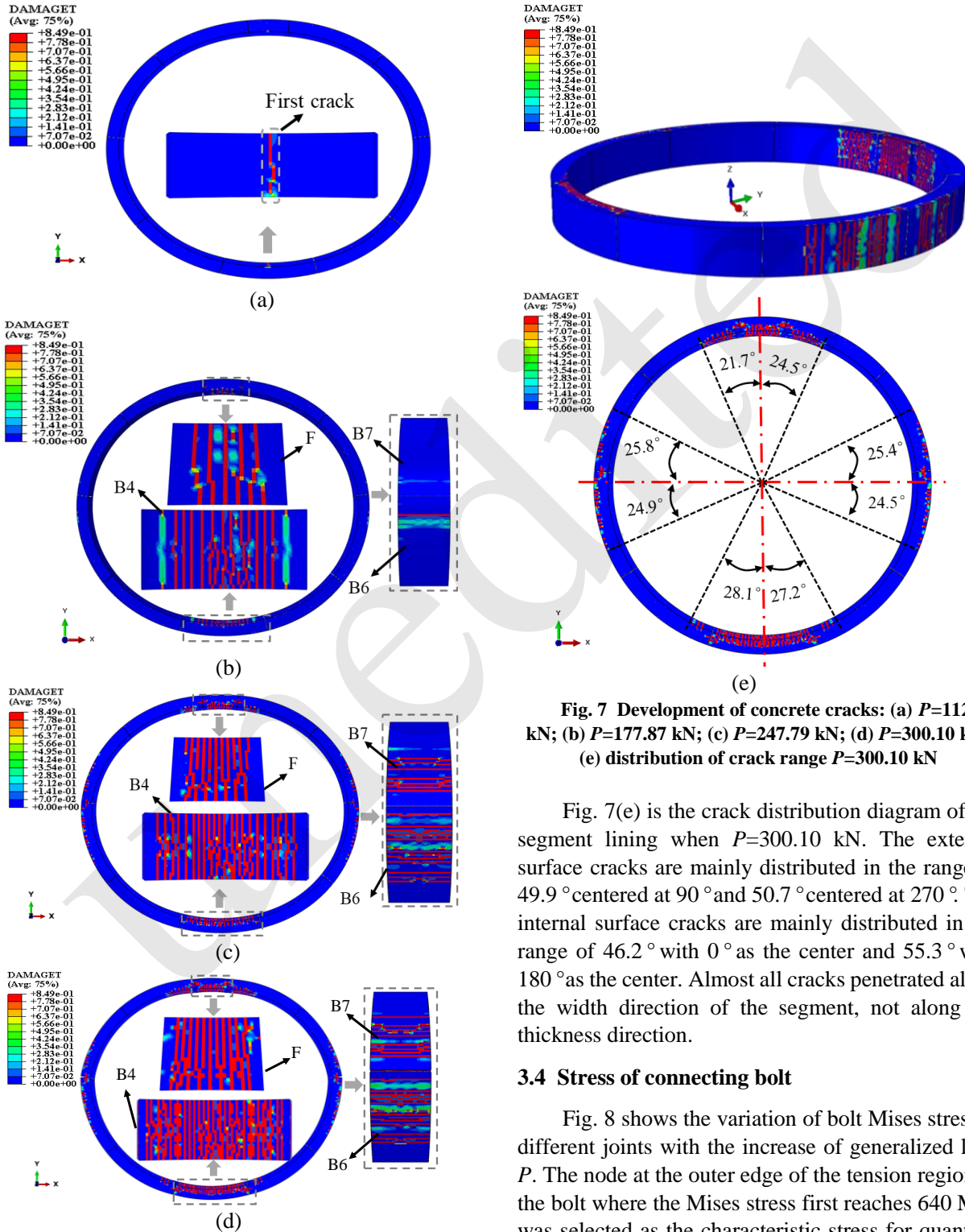| Location	9°/351°	47°/313°	85°/275°	123°/237°	161°/199°
Bending moment (kN·m)	2131/2132	-535.4/-494.1	-2108/-2067	-804.4/-803.4	2289/2235
Axial force (kN)	7617.3/7624.8	8414.3/8373.5	8055.1/7907.2	8534.9/8486.2	8205.8/8131.6

(a)

(b)

(c)

(d)

(e)

Fig. 7 Development of concrete cracks: (a) *P*=112.56 kN; (b) *P*=177.87 kN; (c) *P*=247.79 kN; (d) *P*=300.10 kN; (e) distribution of crack range *P*=300.10 kN

Fig. 7(e) is the crack distribution diagram of the segment lining when *P*=300.10 kN. The external surface cracks are mainly distributed in the range of 49.9° centered at 90° and 50.7° centered at 270°. The internal surface cracks are mainly distributed in the range of 46.2° with 0° as the center and 55.3° with 180° as the center. Almost all cracks penetrated along the width direction of the segment, not along the thickness direction.

3.4 Stress of connecting bolt

Fig. 8 shows the variation of bolt Mises stress at different joints with the increase of generalized load *P*. The node at the outer edge of the tension region of the bolt where the Mises stress first reaches 640 MPa was selected as the characteristic stress for quantita-

tive analysis. As shown in the figure, the variation law of bolt stress at joints of 9 °, 85 °, 161 °, 199 °, 275 ° and 351 °is similar, and all of them eventually yield. The bolts at joints of 47 °, 123 °, 237 °and 313 °did not yield. The stress of the bolts at the joints of 9 °, 85 °, 161 °, 199 ° and 351 °experience a linear increase as the generalized load *P* increases (Stage I in the Fig. 8), a quasi-linear growth (Stage II$_a$), a non-linear increase (Stage II$_b$, Stage III) and a yield phase (Phase IV) in sequence. The bolt yield load is shown in Table 5. Conversely, the bolt stress at the joints of 47 °, 123 °, 237 ° and 313 ° is always in an elastic state, and the maximum stresses are 112.32 MPa, 101.91 MPa, 102.04 MPa and 118.49 MPa, respectively.

Table 5 Bolt yield generalized load

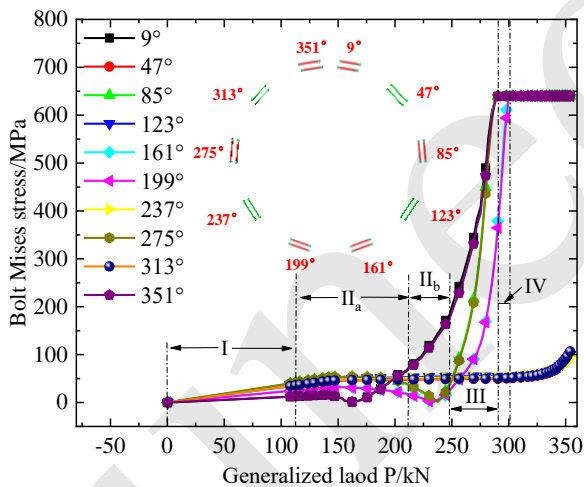| Location	Yield load of bolts /kN	Location	Yield load of bolts /kN
9 °	294.87	351 °	294.87
85 °	290.41	275 °	290.41
161 °	300.10	199 °	300.10

Fig. 8 Stress distribution of bolts

3.5 Stress of tensile rebar

Fig. 9 shows the variation of tensile rebar stress with overload. As depicted in the figure, the rebar stress change in relation to the generalized load is basically similar. Under the state of ultimate bearing capacity, the rebar stress at 180 °is greater than that at other positions. Taking the change of rebar stress at 180 ° as an example, when *P* increases from 0 to 112.56 kN, the rebar stress increases linearly to 12.52 MPa. When *P* increases from 112.56 kN to 247.79

kN, the rebar stress increases slowly and nonlinearly. When *P* increases from 247.79 kN to 300.10 kN, the rebar stress increases rapidly and finally reaches 306.46 MPa. That is, the tensile reinforcement has gone through elastic stage, nonlinear growth stage and rapid growth stage. However, the tensile reinforcement did not reach its yield point at the ultimate state.
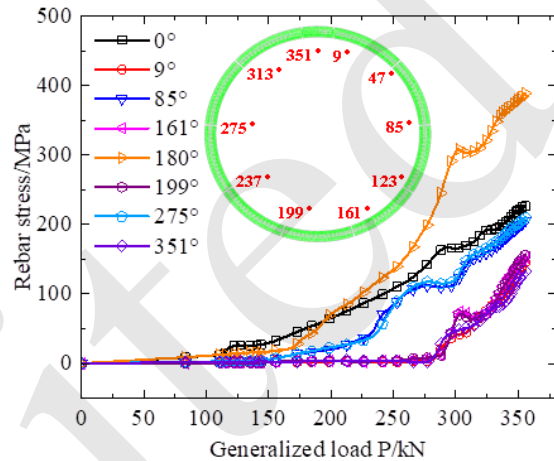

Fig. 9 Tensile rebar stress changes with overload

3.6 Compressive strain of concrete

Fig. 10 (a) shows the distribution of concrete compression damage at *P*=300.10 kN. As depicted in the figure, the concrete on the outside of the 9 °, 161 °, 199 °, 351 °joints and the inside of the 85 °, 275 °joints was crushed. The large-diameter segment has many concrete crush zones, and it is easier to form a geometrically variable system. The crown, invert and haunch of the segment are the weak areas of bearing capacity and special attention should be paid to the overload there.

To ensure the standardization and reliability of data extraction, the feature points for data extraction are the nodes where the principal compressive strain at the joint first reaches a peak, then declines or transforms into tensile strain. As depicted in Fig.10 (b), compared with other joints, the concrete compressive strain at the joints 47 °, 123 °, 237 °and 313 °is much lower, and the concrete does not collapse. As the generalized load *P* increases, the compressive strain of concrete at the joints of 9 °, 85 °, 161 °, 199 °, 275 °and 351 °experiences a linear increase stage, a nonlinear increase stage and a rapid increase stage until crushing. Under the same generalized load, the

concrete compressive strains at 161 °and 199 °of the joints are larger than at other joints. The concrete crushing sequence is 85 ° (275 °), 9 ° (351 °), 161 ° (199 °), and the corresponding concrete crushing generalized loads are 271.94 kN, 288.04 kN, 293.19 kN, respectively.
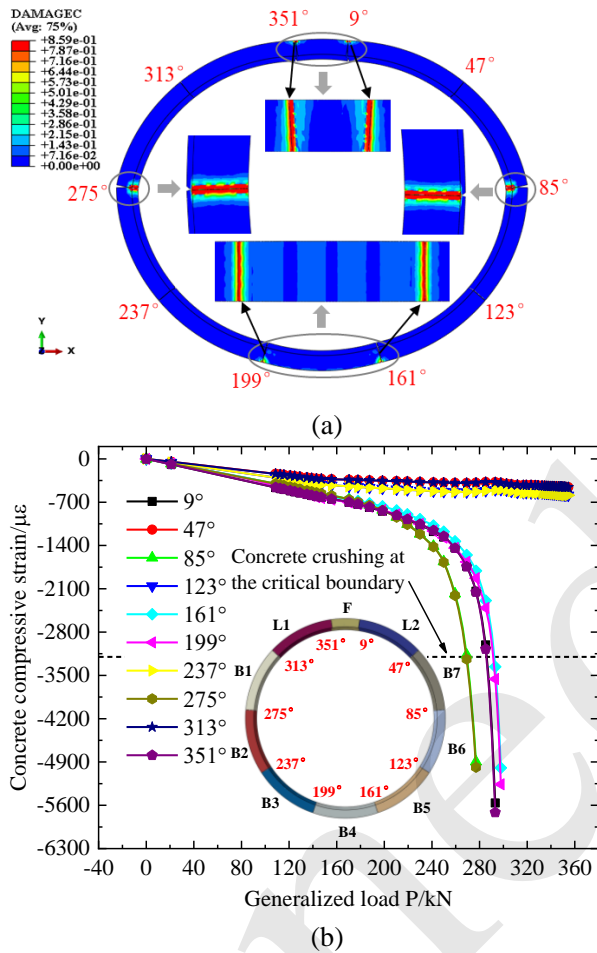

(a)

(b)

Fig. 10 Compressive damage distribution and compressive strain change of segment concrete: (a) Compression distribution of large-diameter segments (DAMAGEC); (b) Change of concrete compressive stress at segment joint

3.7 Longitudinal joint opening

The joints of 9 °, 161 °, 199 °and 351 °are in the outer compression and inner tension state, whereas the joints of 85 °and 275 °are in the outer tension and inner compression state as the generalized load *P* increases. The full section at the 47 °, 123 °, 237 °and

313 °joints is in compression without opening. The joint opening of the segment is calculated according to the following formula:

$$\Delta = \sqrt{(u_{xm} - u_{xn})^2 + (u_{ym} - u_{yn})^2}, \qquad (2)$$

where, Δ is is the opening of the joint; u_{xm} is the displacement of node *m* in the X direction; u_{xn} is the displacement of node *n* in the X direction; u_{ym} is the displacement of node *m* in the Y direction; u_{yn} is the displacement of node *n* in the Y direction.

In Fig. 11, the joint opening extent is plotted against the generalized load *P*. The specified joint opening amount is positive for outer compression and inner tension, otherwise it is negative. From the figure, it can be seen that the joint opening amount first increases linearly and then nonlinearly. In the linear stage, the opening amount of each joint is almost the same under the same bending moment, while in the nonlinear stage the absolute values of joint opening at 85 °and 275 °are greater than those at joints 9 °, 351 °, 161 °and 199 °.

Table 6 shows the opening of the segment joints when the bolts are yielding and when the structure is at its ultimate load state. As can be observed, the joint opening amount at the point where the bolt yield is very close to the joint opening amount at the point where the structural bearing capacity reaches the limit. This indicates that the bearing capacity of the structure will be lost soon after the bolt yields.
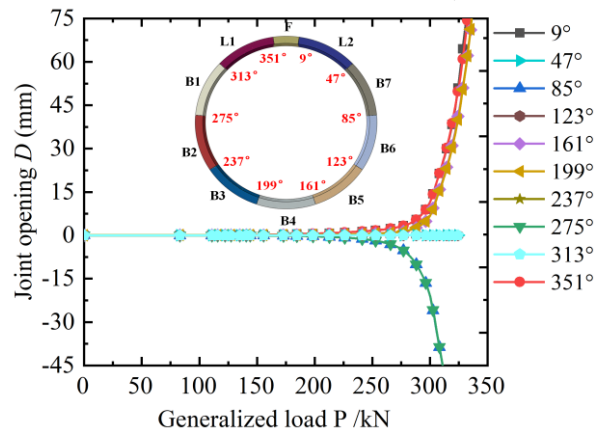

Fig. 11 Segment joint opening

Table 6 Opening amount at different joints of segments

Joint location	Bolt yield load/kN	Opening of bolt at yield δ_1/mm	Opening of structural ultimate load δ_2/mm	δ_1 / δ_2
9 °	294.87	8.16	11.66	69.98%

47 °	--	0	0	--
85 °	290.41	11.66	21.15	55.13%
123 °	--	0	0	--
161 °	300.10	6.95	6.95	100%
199 °	300.10	6.79	6.79	100%
237 °	--	0	0	--
275 °	290.41	11.64	21.08	55.22%
313 °	--	0	0	--
351 °	294.87	8.12	11.54	70.36%

4 Discussion

4.1 Failure mechanism of segment lining of a large diameter shield

The failure process of large-diameter segments is analyzed below to try to clarify how the segment lining gradually cracks the concrete, causes the bolts to yield and finally reaches the ultimate bearing capacity under overload. Three macroscopic performance points are defined here to characterize the development of the progressive failure process of the structure.

Elastic point: The first tensile crack in the segment, or the moment when the compressed concrete first reaches peak stress. Before the elastic point, the material of the structure is in an elastic state, and the structure can return to its original state after unloading.

Yielding point: The moment when the reinforcement of the segment yields in tension or the concrete compression zone collapses, and the connecting bolts of the joints yield or there is crushing of the concrete at the edge of the compression zone. The plastic hinge of the segment can be produced by the yielding of the tensile reinforcement and the crushing of the concrete in the compression zone at this location. The plastic hinge of the joint can be produced by the tensile yield of the connecting bolt and the crushing of the concrete at the edge of the compression zone at this location. A semi-plastic hinge is defined as only one of the connection bolts yielding, the tensile reinforcement yielding, or the concrete crushing. The structure can continue to bear the load after a semi-plastic hinge has been formed.

Ultimate point: The moment when the structure undergoes overall instability or system transformation. The increasing number of plastic hinges in the lining structure makes the original segment lining structure form a variable system and it cannot continue to bear the load.

Fig. 12 shows the formation process of segment macro performance points under the condition of overload. The deformation mechanism of the large-diameter segmental ring at each stage is analyzed as follows. 1) Stage I (OA): all steel bars, bolts and compressed concrete are in an elastic state. At the end of this stage, the first penetrating crack of the segment ring is formed along the width direction of the segment. 2) Stage II (II$_a$: AB; II$_b$: BC): the reinforcement stress, bolt stress, and compressive strain of concrete continuously increase with the increase of load. At this stage, a large number of cracks gradually appear in the segmental ring, until the sharp increase in cracks at point C stops. 3) Stage III (CD): the concrete at the segment joints gradually collapses and the bolts gradually yield. At the end of this stage, the four plastic hinges are completely formed for the large-diameter shield segmental ring, and the structure is transformed into a geometrically variable system. 4) Stage IV (DE): the large-diameter shield segmental ring enters a failure state, the bolts at the joints continue to gradually yield and the concrete has further crushing. Finally, the structure is completely damaged, making it difficult for the structure to continue bearing the load.

Fig.12 illustrates that the transverse deformation increases slowly with the generalized load from the elastic point to the first yield point. After the first semi-plastic hinge is formed in the segment lining structure, the transverse deformation develops rapidly and the internal force is redistributed, then new semi-plastic hinges are formed successively at other joints. It eventually becomes unstable due to the gradual increase in the degree of freedom of the structure. The failure of large-diameter shield tunnel segments begins with the collapse of the joint concrete at the spring line. The plastic hinge formation sequence of the large-diameter segmental ring is 85 ° and 275 ° first, then 9 ° and 351 °, and finally 161 ° and 199 °. That is, the sequence of plastic hinge formation

of large-diameter shield tunnel segment is waist, crown, and invert. Therefore, during the operation of shield tunnels, significant deformation of the structure at the waist should be particularly noted. When cracks appear in the structure, the concrete stress is transferred to the reinforcement, resulting in the rapid development of the transverse deformation of the segment. The corresponding load of the segment in its critical state is shown in Table 7. The load at which the ultimate point is formed is very close to that at which the first yield point is formed. The ultimate bearing capacity of the structure is controlled by the timing of the formation of the first yield point. Therefore, the transverse deformation during the formation of the first semi-plastic hinge (i.e., the first yield point) of the structure is selected as the deformation control value for large-diameter shield tunnel segments, with a value of 128 mm $\approx 8‰D_0$ (D_0 represents the outer diameter of the tunnel).
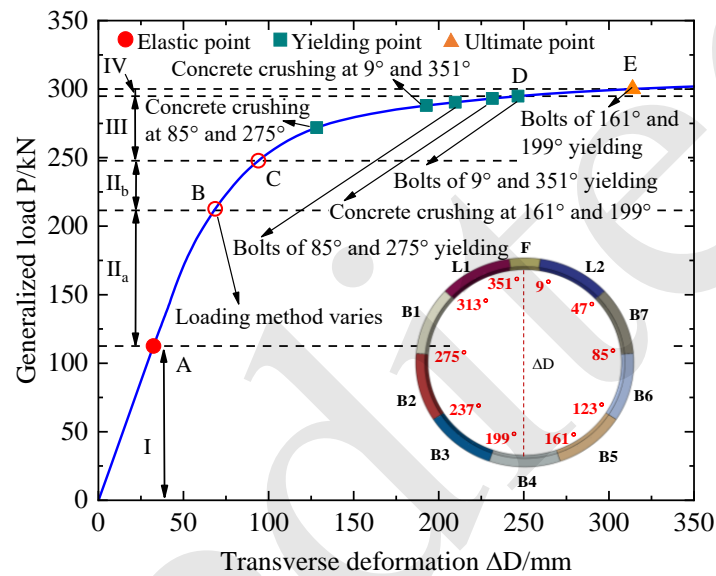

Fig. 12 Formation process of macro performance points

Table 7 Key critical state and corresponding generalized loads

Location	Yield load of bolts /kN	Crushing load of concrete /kN
9°	294.87	288.04
85°	290.41	271.94
161°	300.10	293.19
199°	300.10	293.19
275°	290.41	271.94
351°	294.87	288.04

4.2 Evaluation of integral bearing performance of segmental ring

The structural failure of large-diameter shield tunnel segments is dominated by stability damage, so it is challenging to use a single deformation index to evaluate the bearing performance of segments. When evaluating the bearing performance of the whole ring structure, it is analyzed from the two aspects of structural strength and stiffness. The strength is primarily for segments and joints, while the stiffness is mainly for the whole structure.

The ratio of the generalized load increment to the transverse deformation increment is defined as the stiffness of the segmental ring, which represents the ability of the segmental ring to resist deformation. The stiffness of the segmental ring varies with the overload above, as shown in Fig. 13.

Stage I: The stiffness increases significantly as a result of the numerical instability brought on by the initial calculation iteration. After the segmental ring stiffness is stabilized, it is selected as the initial stiffness of the segmental ring, K_0=30.63 MN/m. When P=112.56 kN, the concrete in the tension zone begins to enter a plastic state, and the stiffness of the segmental ring begins to decrease. Its structural stiffness is K=29.73 MN/m, which is 97.1% of its initial stiffness. The stiffness loss of the segmental ring at this stage is mainly caused by the plastic deformation of the concrete in the tensile zone.

Stage II$_a$: As the load increases, the stiffness of the segmental ring gradually decreases to 24.35 MN/m, which is 79.5% of the initial segmental stiffness. The progressive development of segment cracks is the primary cause of the loss of segmental stiffness in this stage.

Stage II$_b$: During this stage, concrete cracks have increased significantly, and the concrete strain has gradually shifted to bolts and reinforcement. The stiffness of the segmental ring has decreased to K=21.23 MN/m, which is 69.3% of the initial segmental ring stiffness. The reason for the decrease in stiffness at this stage is the sharp increase in segmental ring cracks.

Stage III: The plastic hinges have formed successively in the segmental ring, resulting in a significant decrease in structural stiffness. When P=294.87 kN, the segmental ring stiffness dropped to 1.98 MN/m, which was 6.46% of the initial segmental ring stiffness. The continuous formation of semi-plastic hinges is what causes the stiffness loss of the segmental ring.

Stage IV: The plastic hinges of the segmental ring continue to develop successively, and eventually the structure reaches its ultimate bearing capacity. When P=300.10 kN, the segmental ring stiffness decreases to 0.988 MN/m, which is 3.22% of the initial stiffness. The decrease in stiffness is mainly due to the continuous development of the semi-plastic hinges into complete plastic hinges at this stage.
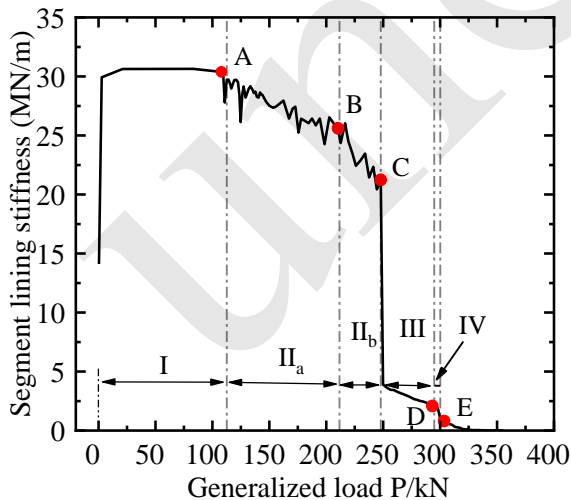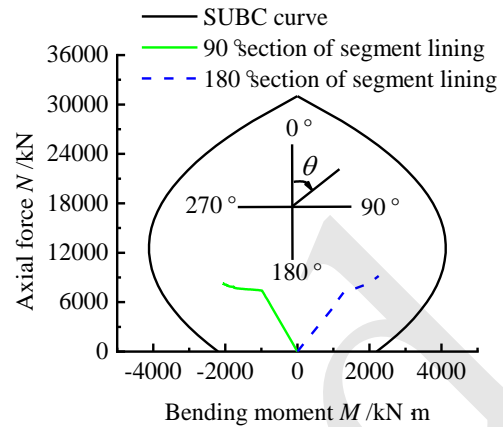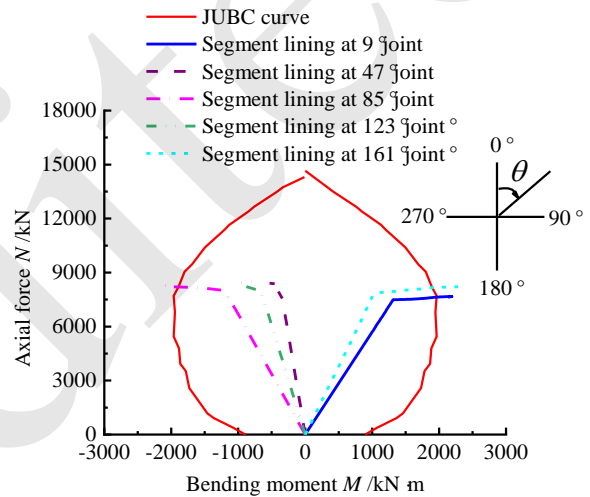

Fig. 13 Changes of stiffness of segmental ring during overload

(a)

(b)

Fig. 14 Distribution of internal force of segment lining and joints and corresponding ultimate bearing capacity: (a) Internal force at maximum positive and negative bending moment of segment and corresponding ultimate bearing capacity; (b) Internal force of joint and corresponding ultimate bearing capacity

The failure of the entire ring structure of the segment is divided into segment failure and joint failure. It is generally considered that the segment joint is a weak part and is more prone to be damaged. However, the stiffness of the joint is relatively low and the internal force of the joint is generally small. Zhang, et al. (2019a) established a theory of compression-bending bearing capacity based on a mechanical model of segment joints. Therefore, based on the segment size, reinforcement and the joint structural parameters of the Wanghai Road Tunnel, the segment ultimate bearing capacity curve (SUBC) and the joint ultimate bearing capacity curve (JUBC) are

calculated. Using these two curves can comprehensively characterize the local flexural bearing capacity of the segment structure. These two kinds of curves are collectively referred to as the flexural bearing capacity characteristic curve of a segment structure.

The internal force at the maximum positive and negative bending moments of the segment section is brought into the segment ultimate bearing capacity curve, as shown in Fig. 14(a). The internal force combination of the segment does not exceed the ultimate bearing capacity of its section, indicating that the segment is not damaged. As shown in Fig. 14(b), the internal force combination of the segment joint is included in the ultimate bearing capacity curve. The internal force combinations of the 9°, 85°, 161° of the joint and their symmetrical locations have exceeded the joint ultimate bearing capacity curve, indicating that these joints have finally been damaged. Since the segmental lining is left and right symmetrical, the corresponding joints have also been damaged. The failure of the large-diameter segment ring lining structure is mainly caused by the loss of the bearing capacity of the joint. After the joint loses its bearing capacity, the overall stiffness and bearing capacity of the structure decrease, and the structure cannot meet the bearing requirements.

5 Conclusions

In this study, a refined 3D finite element analysis was conducted on a large-diameter shield tunnel segment to investigate its transverse deformation behavior and mechanical mechanism under overload. The following conclusions can be drawn:

(1) The transverse deformation of a large-diameter shield segmental ring can be divided into four stages: i) linear growth stage (Stage I); ii) quasi-linear growth stage (Stage II$_a$, Stage II$_b$); iii) nonlinear growth stage (Stage III); iv) failure stage (Stage IV).

(2) During stage I, the reinforcement, bolts and concrete are all in an elastic state, and no crack through occurs. In stage II$_a$ and II$_b$, the stress of bolts, reinforcement, and compressive strain of concrete begin to increase, and a large number of cracks appear in the segment, gradually reducing the stiffness of the segmental ring. In stage III, semi-plastic hinges are formed successively and develop towards complete plastic hinges in the structure, resulting in a sharp decrease in the stiffness of the segmental ring. In

stage IV, the complete plastic hinge of the structure continues to form, and ultimately the structure cannot continue to bear the load. The extensive development of cracks and the complete formation of four plastic hinges are the main reasons for the decrease in stiffness of the segmental ring.

(3) The transverse deformation during the formation of the first semi-plastic hinge (i.e., the first yield point) of the structure is selected as the deformation control value for large-diameter shield tunnel segments and is equal to 8‰ of the segment's outer diameter. This control value can serve as a reinforcement standard for preventing the failure of large diameter shield tunnel segments.

(4) The calculated internal force is substituted into the flexural bearing capacity characteristic curve of the segmental ring and it is discovered that the maximum internal force combination of the segment does not exceed the segment ultimate bearing capacity curve (SUBC). However, the combination of internal forces at 9°, 85°, 161° of the joint and their symmetrical locations about the 0°~180° axis exceeds the joint ultimate bearing capacity curve (JUBC). This indicates that the failure of a large-diameter segmental ring is mainly due to insufficient joint strength, resulting in structural instability. When three or more bolts in the segment ring joint yield, rapid destabilization and failure of the large-diameter segment ring occur.

Although this study conducted a detailed analysis of the failure process of large-diameter segments, it mainly focused on the typical 15 m-level large-diameter shield tunnel with a specific joint structure. Many influencing factors such as partition methods, bolt connection forms, joint details, tunnel depth, and soil types have not been thoroughly investigated. Future research can delve into these influencing factors to develop more applicable deformation control standards for large-diameter shield tunnel segments.

Author contributions

Huai-na WU and Ren-peng CHEN designed the research.

Bin-yong GAO, Cheng-cheng ZHANG, and Meng FAN processed the corresponding data. Bin-yong GAO wrote the first draft of the manuscript. Meng FAN and Chao XIAO helped to organize the manuscript. Huai-na WU and Ren-peng CHEN revised and edited the final version.

Conflict of interest

Bin-yong GAO, Ren-peng CHEN, Huai-na WU, Cheng-cheng ZHANG, Meng FAN, and Chao XIAO declare that they have no conflict of interest.

References

Arnau O, Molins C, 2012. Three dimensional structural response of segmental tunnel linings. *Engineering Structures*, 44:210-221. https://doi.org/10.1016/j.engstruct.2012.06.001

Arnau O, Molins C, 2015. Theoretical and numerical analysis of the three-dimensional response of segmental tunnel linings subjected to localized loads. *Tunnelling and Underground Space Technology*, 49:384-399. https://doi.org/10.1016/j.tust.2015.05.012

Birtel V, Mark P, 2006. Parameterised finite element modelling of RC beam shear failure. [C]// Proceedings of the 19th Annual International ABAQUS Users'Conference. Boston, USA, p.95-108.

Blom CBM, Van Der Horst EJ, Jovanovic PS, 1999. Three-dimensional structural analyses of the shield-driven "green heart" tunnel of the high-speed line south. *Tunnelling and Underground Space Technology*, 14:217–224. https://doi.org/https://doi.org/10.1016/S0886-7798(99)00035-8

Cavalaro SHP, Blom CBM, Walraven JC, et al., 2011. Structural analysis of contact deficiencies in segmented lining. *Tunnelling and Underground Space Technology*, 26(6):734-749. https://doi.org/10.1016/j.tust.2011.05.004

Chang CT, Sun CW, Duann S-W, et al., 2001. Response of a taipei rapid transit system (trts) tunnel to adjacent excavation. *Tunnelling and Underground Space Technology*, 16:151-158. https://doi.org/https://doi.org/10.1016/S0886-7798(01)00049-9

Chen JS, Mo HH, 2008. Mechanical behavior of segment rebar of shield tunnel in construction stage. *Journal of Zhejiang University-SCIENCE A*, 9(7):888-899. https://doi.org/10.1631/jzus.A0720025

Chen J, Mo H, 2009. Numerical study on crack problems in segments of shield tunnel using finite element method. *Tunnelling and Underground Space Technology*, 24(1):91-102. https://doi.org/10.1016/j.tust.2008.05.007

Chen RP, Lin XT, Wu HN, 2019. An analytical model to predict the limit support pressure on a deep shield tunnel face. *Computers and Geotechnics*, 115 https://doi.org/10.1016/j.compgeo.2019.103174

Chen RP, Chen S, Wu HN, et al., 2020. Investigation on deformation behavior and failure mechanism of a segmental ring in shield tunnels based on elaborate numerical simulation. *Engineering Failure Analysis*, 117 https://doi.org/10.1016/j.engfailanal.2020.104960

Chen RP, Meng FY, Li Z, et al., 2016. Investigation of response of metro tunnels due to adjacent large excavation and protective measures in soft soils. *Tunnelling and Underground Space Technology*, 58:224-235. https://doi.org/10.1016/j.tust.2016.06.002

Dassault Systèmes, D, 2016. Abaqus analysis user's guide. Technical Report Abaqus 6.14 Documentation, Simulia Corp

Ding WQ, Yue ZQ, Tham LG, et al., 2003. Analysis of shield tunnel. *International Journal for Numerical and Analytical Methods in Geomechanics*, 28(1):57-91. https://doi.org/10.1002/nag.327

Ding W, Jin Y, Zhao W, et al., 2014. A computational method for ground penetrating shield tunnel. *Tunneling and Underground Construction*, Presented at the Geo-Shanghai 2014, American Society of Civil Engineers, Shanghai, China, pp. 227–236. https://doi.org/10.1061/9780784413449.023

Du X, Jin L, Ma G, 2014. Numerical simulation of dynamic tensile-failure of concrete at meso-scale. *International Journal of Impact Engineering*, 66:5-17. https://doi.org/10.1016/j.ijimpeng.2013.12.005

Feng K, He C, Qiu Y, et al., 2018. Full-scale tests on bending behavior of segmental joints for large underwater shield tunnels. *Tunnelling and Underground Space Technology*, 75:100-116. https://doi.org/10.1016/j.tust.2018.02.008

Gong C, Ding W, 2018. A computational framework to predict the water‑leakage pressure of segmental joints in underwater shield tunnels using an advanced finite element method. *International Journal for Numerical and Analytical Methods in Geomechanics*, 42(16):1957-1975. https://doi.org/10.1002/nag.2839

Guo W, Feng K, Zhou Y, et al., 2023. Full-scale test and numerical modeling on deformation and damage behavior of segmental joints under ultimate compression-bending load. *Engineering Structures*, 279: 115648. https://doi.org/10.1016/j.engstruct.2023.115648

Han L, Ye GL, Chen J-J, et al., 2017. Pressures on the lining of a large shield tunnel with a small overburden: A case study. *Tunnelling and Underground Space Technology*, 64:1-9. https://doi.org/10.1016/j.tust.2017.01.008

He C, Feng K, 2021. Integrated analysis method for shield tunnel structure with large cross-section. *Tunnel Construction*, 41(11): 1827-1848 (in Chinese)

Huang X, Huang H, Zhang J, 2012. Flattening of jointed shield-driven tunnel induced by longitudinal differential settlements. *Tunnelling and Underground Space Technology*, 31:20-32. https://doi.org/10.1016/j.tust.2012.04.002

Huang Z, Zhang CL, Ma SK, et al., 2021. Study of the mechanical behaviour and damage characteristics of three new types of joints for fabricated rectangular tunnels using a numerical approach. *Tunnelling and Underground Space Technology*, 118 https://doi.org/10.1016/j.tust.2021.104184

Jin Y, Ding W, Yan Z, et al., 2017. Experimental investigation of the nonlinear behavior of segmental joints in a water-conveyance tunnel. *Tunnelling and Underground Space Technology*, 68:153-166. https://doi.org/10.1016/j.tust.2017.05.018

Koyama Y, Nishimura T, 1998. Design of lining segment of shield tunnel using a beam-spring model. *Quarterly Report of RTRI (Railway Technical Research Institute)*, 39(1):23-27 (in Japanese).

Lee KM, Ge XW, 2001. The equivalence of a jointed shield-driven tunnel lining to a continuous ring structure. *Canadian Geotechnical Journal*, 38(3):461-483. https://doi.org/10.1139/t00-107

Li P, Du SJ, Ma XF, et al., 2014. Centrifuge investigation into the effect of new shield tunnelling on an existing underlying large-diameter tunnel. *Tunnelling and Underground Space Technology*, 42:59-66. https://doi.org/10.1016/j.tust.2014.02.004

Li X, Yan Z, Wang Z, et al., 2015. A progressive model to simulate the full mechanical behavior of concrete segmental lining longitudinal joints. *Engineering Structures*, 93:97-113. https://doi.org/10.1016/j.engstruct.2015.03.011

Li Z, Soga K, Wright P, 2016. 3D finite element analysis of the behaviour of cross passage between cast-iron tunnels. *Canadian Geotechnical Journal*, 53:930–945. https://doi.org/https://doi.org/10.1139/cgj-2015-027

Liao SM, Peng FL, Shen S-L, 2008. Analysis of shearing effect on tunnel induced by load transfer along longitudinal direction. *Tunnelling and Underground Space Technology*, 23(4):421-430. https://doi.org/10.1016/j.tust.2007.07.001

Liu J, Shi C, Gong C, et al., 2022. Investigation of ultimate bearing capacity of shield tunnel based on concrete damage model. *Tunnelling and Underground Space Technology*, 125 https://doi.org/10.1016/j.tust.2022.104510

Liu X, Bai Y, Yuan Y, et al., 2015. Experimental investigation of the ultimate bearing capacity of continuously jointed segmental tunnel linings. *Structure and Infrastructure Engineering*, 12(10):1364-1379. https://doi.org/10.1080/15732479.2015.1117115

Liu X, Dong Z, Bai Y, et al., 2017a. Investigation of the structural effect induced by stagger joints in segmental tunnel linings: First results from full-scale ring tests. *Tunnelling and Underground Space Technology*, 66:1-18. https://doi.org/10.1016/j.tust.2017.03.008

Liu X, Jiang Z, Yuan Y, et al., 2017b. Experimental investigation of the ultimate bearing capacity of deformed segmental tunnel linings strengthened by epoxy-bonded steel plates. *Structure and Infrastructure Engineering*, 14(6):685-700. https://doi.org/10.1080/15732479.2017.1354892

Liu X, Liu Z, Ye Y, et al., 2018. Mechanical behavior of quasi-rectangular segmental tunnel linings: Further insights from full-scale ring tests. *Tunnelling and Underground Space Technology*, 79:304-318. https://doi.org/10.1016/j.tust.2018.05.016

Liu X, Zhang Y, Bao Y, 2020. Full-scale experimental investigation on stagger effect of segmental tunnel linings. *Tunnelling and Underground Space Technology*, 102 https://doi.org/10.1016/j.tust.2020.103423

Lu L, Lu X, Fan P, 2011. Full-ring experimental study of the lining structure of shanghai changjiang tunnel. *Journal of Civil Engineering and Architecture*, 5(1934-7359):732-739. https://doi.org/https://doi.org/10.17265/1934-7359/2011.08.007

Meng FY, Chen RP, Liu SL, et al., 2021. Centrifuge

modeling of ground and tunnel responses to nearby excavation in soft clay. *Journal of Geotechnical and Geoenvironmental Engineering*, 147(3) https://doi.org/10.1061/(asce)gt.1943-5606.0002473

Meng FY, Chen RP, Xu Y, et al., 2022. Contributions to responses of existing tunnel subjected to nearby excavation: A review. *Tunnelling and Underground Space Technology*, 119:104195. https://doi.org/10.1016/j.tust.2021.104195

Moradloo AJ, Adib A, Pirooznia A, 2019. Damage analysis of arch concrete dams subjected to underwater explosion. *Applied Mathematical Modelling*, 75:709-734. https://doi.org/10.1016/j.apm.2019.04.064

Murakami H, Koizumi, 1978. A study on load bearing capacity and mechanics of shield segment ring. *Proceedings of JSCE*, 272:103–115 (in Japanese). https://doi.org/https://doi.org/10.2208/jscej1969.1978.272_103

Nakamura H, Kubota T, Furukawa M, et al., 2003. Unified construction of running track tunnel and crossover tunnel for subway by rectangular shape double track cross-section shield machine. *Tunnelling and Underground Space Technology*, 18(2-3):253-262.
https://doi.org/10.1016/s0886-7798(03)00034-8

Qiu Y, Hu X, Walton G, et al., 2021. Full scale tests and a progressive failure model to simulate full mechanical behavior of concrete tunnel segmental lining joints. *Tunnelling and Underground Space Technology*, 110 https://doi.org/10.1016/j.tust.2021.103834

SAC/TC (Technical Committee on Steel of Standardization Committee of China), 2022. Test methods of steel for reinforcement of concrete, GB/T 28900-2022. National Standards of the People's Republic of China

Shen SL, Yan T, Zhou A, 2023a. Estimating locations of soil–rock interfaces based on vibration data during shield tunnelling. *Automation in Construction*, 150 https://doi.org/10.1016/j.autcon.2023.104813

Shen SL, Zhang N, Zhou A, 2023b. Investigation of disc cutter wear during shield tunnelling in weathered granite: A case study. *Tunnelling and Underground Space Technology*, 140 https://doi.org/10.1016/j.tust.2023.105323

Wang F, Shi J, Huang H, et al., 2020. Modified analytical solution of shield tunnel lining considering nonlinear bending stiffness of longitudinal joint. *Tunnelling and Underground Space Technology*,

106 https://doi.org/10.1016/j.tust.2020.103625

Wang M, Dong Y, Yu L, et al., 2019. Experimental and numerical researches of precast segment under radial dislocation conditions. *Tunnelling and Underground Space Technology*, 92 https://doi.org/10.1016/j.tust.2019.103055

Wei G, Feng F, Hu C, et al., 2022. Mechanical performances of shield tunnel segments under asymmetric unloading induced by pit excavation. *Journal of Rock Mechanics and Geotechnical Engineering*, 15(6):1547-1564. https://doi.org/10.1016/j.jrmge.2022.08.010

Wu HN, Shen SL, Chen RP, et al., 2020. Three-dimensional numerical modelling on localised leakage in segmental lining of shield tunnels. *Computers and Geotechnics*, 122 https://doi.org/10.1016/j.compgeo.2020.103549

Wu HN, Chen S, Chen RP, et al., 2022. Deformation behaviors and failure mechanism of segmental rc lining under unloading condition. *Tunnelling and Underground Space Technology*, 130 https://doi.org/10.1016/j.tust.2022.104687

Yan Q, Xu Y, Zhang W, et al., 2018. Numerical analysis of the cracking and failure behaviors of segmental lining structure of an underwater shield tunnel subjected to a derailed high-speed train impact. *Tunnelling and Underground Space Technology*, 72:41-54.
https://doi.org/10.1016/j.tust.2017.11.002

Yan T, Shen SL, Zhou A, 2022. Identification of geological characteristics from construction parameters during shield tunnelling. *Acta Geotechnica*, 18(1):535-551. https://doi.org/10.1007/s11440-022-01590-w

Yan T, Shen SL, Zhou A, 2023. Gfii: A new index to identify geological features during shield tunnelling. *Tunnelling and Underground Space Technology*, 142 https://doi.org/10.1016/j.tust.2023.105440

Yang F, Cao SR, Qin G, 2020. Simplified spring models for concrete segmental lining longitudinal joints with gaskets. *Tunnelling and Underground Space Technology*, 96 https://doi.org/10.1016/j.tust.2019.103227

Yuan Y, Jiang X, Liu X, 2013. Predictive maintenance of shield tunnels. *Tunnelling and Underground Space Technology*, 38:69-86. https://doi.org/10.1016/j.tust.2013.05.004

Zhang DM, Chen S, Wang RC, et al., 2021. Behaviour of a large-diameter shield tunnel through multi-layered strata. *Tunnelling and Underground*

Space *Technology*, 116
https://doi.org/10.1016/j.tust.2021.104062

Zhang L, Feng K, Gou C, et al., 2019a. Failure tests and bearing performance of prototype segmental linings of shield tunnel under high water pressure. *Tunnelling and Underground Space Technology*, 92
https://doi.org/10.1016/j.tust.2019.103053

Zhang L, Feng K, Li M, et al., 2019b. Analytical method regarding compression-bending capacity of segmental joints: Theoretical model and verification. *Tunnelling and Underground Space Technology*, 93
https://doi.org/10.1016/j.tust.2019.103083

Zhang L, Feng K, Xu P, et al., 2020. Refined three‐dimensional numerical model for segmental joint and its application. *Structural Concrete*, 21(4):1612-1624.
https://doi.org/10.1002/suco.201900550

Zhang L, Feng K, He C, et al., 2023a. Numerical investigation of the compression–bending stiffness of segmental joints with different types of joint surfaces. *Tunnelling and Underground Space Technology*, 132
https://doi.org/10.1016/j.tust.2022.104898

Zhang N, Shen SL, Zhou A, 2023b. A new index for cutter life evaluation and ensemble model for prediction of cutter wear. *Tunnelling and Underground Space Technology*, 131
https://doi.org/10.1016/j.tust.2022.104830

Zhang W, Qi J, Zhang G, et al., 2022. Full-scale experimental study on failure characteristics of the key segment in shield tunnel with super-large cross-section. *Tunnelling and Underground Space Technology*, 129
https://doi.org/10.1016/j.tust.2022.104671

Zhao H, Liu X, Bao Y, et al., 2017. Nonlinear simulation of tunnel linings with a simplified numerical modelling. *Structural Engineering and Mechanics*, 61(5):593-603.
https://doi.org/10.12989/sem.2017.61.5.593

中文概要：

题　目： 大直径盾构隧道管片环力学失效性能研究

作　者： 高斌勇[1,2]，陈仁朋[1,2]，吴怀娜[1,2]，张称星[1,2]，凡猛[1,2]，肖超[3]

机　构： [1]湖南大学，地下空间先进技术研究中心，中国长沙，410082；[2]湖南大学，建筑安全与节能教育部重点实验室，中国长沙，410082；[3]中国建筑第五工程局有限公司，中国长沙

目　的： 随着大直径盾构隧道逐步投入运营，隧道周边的开挖、超载等施工活动导致隧道变形渗漏水及失效问题日益突出。当前对盾构隧道管片衬砌的变形破坏机理和控制标准研究主要集中于小直径隧道。大直径盾构隧道管片直径大、分块多、接头刚度弱等特点，其变形失效机理与小直径管片存在差异，由此缺乏相应变形控制标准。因此，针对大直径盾构隧道管片衬砌开展变形失效机制研究至关重要。

创新点： 1.通过建立精细化数值模型，分析了大直径盾构隧道管片环的变形失效机理；2.提出了适用于大直径盾构隧道管片的变形控制标准。

方　法： 1.通过数值模拟，分析了大直径盾构隧道管片环的横向变形响应(图2和12)；2.通过将计算的管片内力结果带入已有的压弯承载力理论中，分析大直径管片环失效特征(图14)。

结　论： 1.大直径盾构隧道管片环的横向变形可分为4个阶段：i)线性增长阶段(阶段I)，ii)拟线性增长阶段(阶段II_a和II_b)，iii)非线性增长阶段(阶段III)，iv)破坏阶段(阶段IV)；2.阶段I，钢筋、螺栓和混凝土均处于弹性状态，未发生裂缝贯通。阶段II_a和II_b阶段，螺栓、钢筋的应力和混凝土的压应变开始增大，管片出现大量裂缝，管片环的刚度逐渐降低。阶段III，半塑性铰相继形成，并在结构中向完整塑性铰发展，导致管片环刚度急剧下降。阶段IV，结构的完整塑性铰相继形成，最终结构不能继续承受荷载。裂缝的大量发展和四个塑性铰的完全形成是导致管片环刚度降低的主要原因；3.选取大直径盾构隧道管片在形成第一个半塑性铰(即第一屈服点)时的横向变形，即管片外径的8‰作为变形控制值。该值可作为防止大直径盾构隧道管片破坏的加固标准；4.将计算得到的内力代入管片环的抗弯承载力特征曲线中，发现管片的最大内力组合不超过管片极限承载力曲线(SUBC)。而接头9°、85°、161°及其沿0°~180°轴对称位置的内力组合超过接头极限承载力曲线(JUBC)。这说明大直径管片环的破坏主要是由于接头强度不足导致结构失稳。当管片环接头中的三个或三个以上螺栓屈服时，大直径管片环就会迅速失稳破坏。

关键词： 有限元模型；横向变形响应；上方超载；塑性铰；抗弯承载力